

PAPER

Perfusion directed 3D mineral formation within cell-laden hydrogels

To cite this article: Stephen W Sawyer et al 2018 Biofabrication 10 035013

View the article online for updates and enhancements.

Related content

- <u>Conductive gelatin methacrylate-poly(aniline) hydrogel for cell encapsulation</u>
 Stephen W Sawyer, Ping Dong, Sarah Venn et al.
- An in vitro vascular chip using 3D printingenabled hydrogel casting
 Liang Yang, Shivkumar Vishnempet
 Shridhar, Melissa Gerwitz et al.
- A fast-degrading thiol-acrylate based hydrogel for cranial regeneration
 A M Emmakah, H E Arman, J C Bragg et al.



Biofabrication



RECEIVED 26 January 2018

REVISED

3 June 2018

ACCEPTED FOR PUBLICATION 8 June 2018

PUBLISHED 28 June 2018

PAPER

Perfusion directed 3D mineral formation within cell-laden hydrogels

Stephen W Sawyer¹, Shivkumar Vishnempet Shridhar¹, Kairui Zhang¹, Lucas D Albrecht¹, Alex B Filip¹, Jason A Horton² and Pranav Soman¹

- Department of Biomedical and Chemical Engineering, Syracuse University, Syracuse, NY, United States of America
- ² Department of Orthopedic Surgery, SUNY Upstate Medical University, Syracuse, NY, United States of America

E-mail: psoman@syr.edu

Keywords: hydrogel, gelatin methacrylate, cell encapsulation, mineral formation, tissue engineering, perfusion, bioreactor Supplementary material for this article is available online

Abstract

Despite the promise of stem cell engineering and the new advances in bioprinting technologies, one of the major challenges in the manufacturing of large scale bone tissue scaffolds is the inability to perfuse nutrients throughout thick constructs. Here, we report a scalable method to create thick, perfusable bone constructs using a combination of cell-laden hydrogels and a 3D printed sacrificial polymer. Osteoblast-like Saos-2 cells were encapsulated within a gelatin methacrylate (GelMA) hydrogel and 3D printed polyvinyl alcohol pipes were used to create perfusable channels. A custom-built bioreactor was used to perfuse osteogenic media directly through the channels in order to induce mineral deposition which was subsequently quantified via micro-CT. Histological staining was used to verify mineral deposition around the perfused channels, while COMSOL modeling was used to simulate oxygen diffusion between adjacent channels. This information was used to design a scaled-up construct containing a 3D array of perfusable channels within cell-laden GelMA. Progressive matrix mineralization was observed by cells surrounding perfused channels as opposed to random mineral deposition in static constructs. Micro-CT confirmed that there was a direct relationship between channel mineralization within perfused constructs and time within the bioreactor. Furthermore, the scalable method presented in this work serves as a model on how large-scale bone tissue replacement constructs could be made using commonly available 3D printers, sacrificial materials, and hydrogels.

Introduction

One of the largest barriers to engineering a large-scale bone tissue replacement is the ability to supply essential nutrients throughout the entire construct. Since hypoxia and necrosis occur within cells that lie outside of the natural diffusion range of 200–300 μ m, proper vasculature must be available within the replacement tissue to ensure graft viability [1–3]. In traditional static culture systems, nutrient diffusion, and therefore mineralization and cellular viability, is limited to the outer 200–300 μ m of the construct while deeper regions of the system remain hypoxic [4, 5].

In an attempt to increase nutrient diffusion into engineered scaffolds, a variety of means such as solvent casting, particulate leaching, phase separation, gas foaming, emulsion freeze drying, and fiber meshes have been used to generate a wide range of porous scaffolds [6–9]. While these particular methods have

been shown to enhance mass transfer within the machined constructs as well as improve cell seeding, cell proliferation, and construct mineralization, they unfortunately have not provided a complete solution. In particular, these methods do not provide the precise control over pore parameters needed for larger tissue constructs, often resulting in inhomogeneous cellular densities and outcome measures that are hard to predict. Furthermore, as these methods typically require harsh solvents and high temperatures, incorporating live cells during fabrication is near impossible [9–11]. Alternatively, the encapsulation of osteogenic cells within biocompatible hydrogel bioinks such as collagen, alginate, and gelatin allows for a uniform and controlled distribution of cells in situ [12-19]. However, the absence of macroporous voids in the cellladen hydrogel constructs present similar nutrient diffusion limitations [3]. Additionally, although the cell friendly hydrogel provides an environment which is able to closely mimic the natural extracellular matrix, their weak mechanical stability provides yet another obstacle for their use in bone tissue engineering.

Recently, 3D printing technologies have enabled the creation of user-defined channels within cell-laden hydrogels through the extrusion of bioinks in a layer-by-layer manner alongside co-printed sacrificial materials [20–27]. Post-print, the sacrificial material is removed via non-toxic means, resulting in user-defined channels within bulk gels. However, methods such as this require custom-made bioprinters with specialized control hardware and software as well as tunable viscoelastic bioinks that must be specifically matched with the printing parameters. While perfusion of these constructs with nutrients is possible, the systems used are difficult to scale, thereby limiting their usage in a clinical setting.

A simpler, and readily scalable, fabrication method is one that combines the casting of cell-laden hydrogels around pre-fabricated 3D printed structures containing sacrificial materials. In this work, we utilize an unmodified, commercially available 3D printer and water soluble sacrificial material (PVA) to establish perfusable channels within the center of a diffusion limited, structurally supported GelMA hydrogel laden with osteoblast-like cells. The construct is designed to have one inlet and one outlet that provides a direct interface between the cell-laden GelMA and perfusion of nutrients via a scalable, pump-driven bioreactor system. The simple horizontal channel geometry provides a robust method with which to analyze the influence of long-term (4 week) perfusion of osteogenic media on the viability and function of encapsulated cells. Additionally, COMSOL modeling of oxygen diffusion is used to determine optimal spacing between adjacent 3D printed channels, allowing for the design to be scaled up into a perfusable, 5 pipe array.

Materials and methods

3D printing of frames and pipes

Acrylonitrile butadiene styrene (ABS) thermoplastic frames with inner dimensions of 9 mm long \times 6 mm wide \times 3 mm deep containing 1 mm holes along the construct peripheries and sacrificial polyvinyl alcohol (PVA, 400 μ m diameter) pipes were printed using a commercially available MakerBot Replicator 2 3D printer (MakerBot) (figure 1(A)).

Design and fabrication of polycarbonate bioreactor

Polycarbonate bioreactors were machined from clear, autoclavable, scratch and UV resistant polycarbonate sheets (McMaster-Carr) (figures 1(D)–(F)). Briefly, pre-milled polycarbonate blanks were machined in a MT300 Pro CNC Milling Center (AutoMateCNC) to create both the bottom bioreactor base and it's corresponding top plate (figures S1–2 are available online at stacks.iop.org/BF/10/035013/mmedia).

The bottom bioreactor base plate contained four wells approximately 13 mm long \times 9 mm wide \times 3 mm deep surrounded by 10 screw holes machined using a #43 drill bit. Vertical holes for perfusion along the periphery of the base plate were machined using a #52 (outer) and #72 (inner) drill bit for 21G needle (Thermo Fisher Scientific) insertion. Top plates contained screw holes machined using a #34 drill bit. To ensure a water-tight seal between the polycarbonate base and top, a polydimethylsiloxane gasket (PDMS, Ellsworth Adhesives) mixed in a 1:4 ratio was cured at 60 °C for 24 h and inserted between the base and top sections.

Gelatin methacrylate (GelMA) synthesis

20% (w/v) gelatin methacrylate (GelMA) prepolymer solution used for cellular encapsulation was synthesized according to our previous work [28]. Briefly, porcine skin gelatin (Sigma-Aldrich) was mixed at 10% (w/v) in phosphate buffered saline (PBS, Thermo Fisher Scientific) and reacted with methacrylic anhydride (Sigma-Aldrich). After dialysis and lyophilization, GelMA macromer was stored at -80 °C until needed. Prior to cellular encapsulation, GelMA macromer was combined with PBS and 0.25% UV photo-initiator Irgacure 2959 (Specialty Chemicals) to form the prepolymer solution and sterile filtered using a $0.20~\mu m$ filter (Corning).

Cell culture and perfusion setup

Human osteosarcoma cells (Saos-2, ATCC), commonly used to represent the early stages of osteogenesis [29], were chosen as osteoblast analogs for our model system. Dulbecco's modification of eagle's media (DMEM, Life Technologies) supplemented with 1% Glutamax (Life Technologies), 1% penicillinstreptomycin (Life Technologies), and 10% fetal bovine serum (FBS lot G12102, Atlanta Biologicals) was used as the base media for Saos-2 culture. Cells were maintained at 37 °C in a humidified, 5% CO₂ atmosphere and passaged prior to any new experiment. In order to chemically induce Saos-2 cells to produce mineral, the base media was supplemented with 100 μ M L-ascorbic acid-2-phosphate (AA2P, Sigma-Aldrich), 5 mM β -glycerophosphate (BGP, Sigma-Aldrich), and 10 nM dexamethasone (DEX, Sigma-Aldrich).

Prior to *in situ* polymerization, approximately 1×10^6 cells were suspended in 20% (w/v) GelMA to create a 15% (w/v) solution (162 μ l final volume), and transferred to the 3D printed hybrid ABS frame/PVA pipe construct via dropwise pipetting (figure 1(B)). After the construct was filled, the cell-GelMA solution was UV cured for 1 min 20 s at approximately 5 mW cm⁻² via a Hamamatsu LED Controller (Hamamatsu C11924-51; Hamamatsu Photonics K. K., Japan). PVA pipes were eluted from the constructs by incubation for 24 h in warmed media (figure 1(C)).

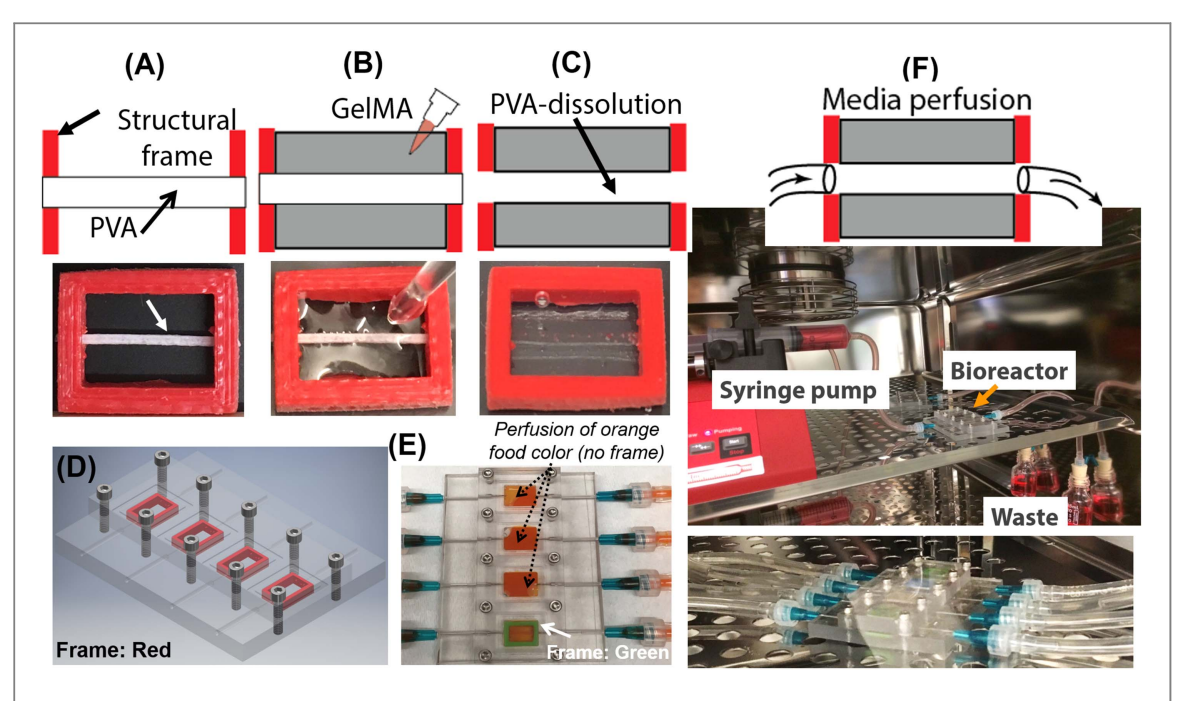


Figure 1. Design and performance testing of 3D printed construct and bioreactor apparatus. Schematic and representative images of the mechanically supportive ABS frame with inserted pipe before (A) and after (B) photopolymerization of GelMA, and after dissolution of the sacrificial PVA pipe (C). Schematic image of a two-piece polycarbonate bioreactor containing a PDMS gasket between layers (D) and leakage test of polycarbonate bioreactor showing liquid-tight seal in machined device (E). Complete bioreactor setup inside a standard cell culture incubator (F).

Constructs destined for static culture conditions remained in 12-well culture dishes, with media renewed every 2–3 days. Constructs destined for perfusion conditions were transferred and press fit within the polycarbonate bioreactor base (figures 1(D), (E)). Construct perfusion was maintained using a syringe pump system (NE-300 Just Infusion TM, New Era) at $0.2 \,\mu l \, h^{-1}$ per well, for up to 28 days (figure 1(F)). Syringes were replaced as needed during the course of the experiments.

Cellular viability

Cell viability of encapsulated Saos-2 cells was evaluated using a Live/Dead assay for two time points: 1 day after encapsulation and 14 days after either perfusion or static culture using osteogenic media. Samples to be evaluated were sliced into 1 mm thick sections and transferred into culture media supplemented with calcein-AM (live, 1:2000 dilution, Life Technologies) and ethidium homodimer (dead, 1:500 dilution, Life Technologies) for one hour prior to imaging.

Micro-CT analysis

Constructs were removed from the bioreactor intact, fixed in formaldehyde (4% for 24 h), washed in PBS, and placed lengthwise in a 16 mm diameter sample holder for micro-CT imaging (micro-CT 40, Scanco Medical AG, Brüttisellen, Switzerland). Foam spacers were placed between samples, which were kept hydrated with PBS. Samples were imaged at a $16-20~\mu m$ isotropic voxel resolution (55 kV, 145 mA, 200 ms integration time). After scanning, mineralized

tissue volume (bone volume, BV) and density (BMD) were calculated by applying a lower global threshold (166 mg HA cm⁻³) to the image, which was digitally contoured to isolate the entire length of the perfusion channel from the bulk construct mass (figure S3). Thickness of the mineralized matrix surrounding the perfusion channel was calculated using the 2D section morphology tool in BoneJ [30]. Briefly, the reconstructed micro-CT images (.isq files) were imported into ImageJ, cropped to isolate the perfusion channel, and a global threshold of 166 mg HA cm⁻³ was applied prior to running BoneJ. The BoneJ plugin then calculates an average 'cortical thickness' for each image slice, which corresponds to mineral wall thickness in this model. Consistency in thresholding between ImageJ and Scanco software was ensured by importing a scan of the Scanco hydroxyapatite (HA) quality control phantom into ImageJ, and plotting greyscale (ImageJ) values versus HA density. However, based on the fact that the structural organization and chemical constitution of the deposited mineral cannot be verified via micro-CT, the cell-mediated deposition is referred to as 'mineral' in the subsequent text.

Histological analysis

Perfused samples were prepared for histological analysis via standard snap freezing protocols. Briefly, samples were fixed in 4% formaldehyde for 24 h before treatment with a 30% sucrose in PBS solution for 48 h. After sucrose treatment, samples were embedded in tissue freezing medium (Electron Microscopy Sciences) and frozen over dry ice. Sections (10 μ m

thick) were cut on a Leica CM3050 cryostat (Leica Biosystems, Germany) and mounted on lysine coated SuperFrost Plus slides. Cover-slipped and stained sections were imaged using a Nikon Eclipse E-400 microscope (Nikon Corporation).

Hematoxylin and eosin (H&E) staining

Sections were stained by standard H&E procedure using Mayer's Hematoxylin and Eosin/Phloxine solutions (Electron Microscopy Sciences). Sections were then dehydrated through an ethanol series, cleared in xylene, and cover-slipped with Permount (Fisher Scientific) for imaging. Imaged sections were analyzed via ImageJ (NIH) for cell quantification.

Alizarin red S staining

Calcium mineral deposition was visualized using 40 mM Alizarin Red S solution (4.1 pH, Sigma). After staining for 5 min, slides were washed in deionized water and mounted and imaged as previously described.

ImageJ box plot analysis

H&E images were imported into ImageJ and analyzed via a box analysis for cell quantification. Briefly, images were converted to binary via automatic thresholding and values representing cells were recorded in boxed increments of $325 \, \mu \text{m}^2$ away from the edge of the channel lumen. For each image, three different directions were analyzed away from the central channel.

COMSOL modeling

COMSOL was first used to model oxygen diffusion within cell-laden GelMA constructs between adjacent channels spaced 1 mm apart (edge-to-edge). Two domains were considered. Domain 1 represented the primary flow of nutrients supplied from the inlet reservoir and was solved using Navier-Stokes steady state flow analysis. Domain 2 represented the diffusion of media and consumption by cells, and was solved by diffusion-consumption analysis using Michaelis-Menten rate laws. The 'Reacting Flow of Porous Media' module in COMSOL was used to plot steady state oxygen diffusion within cell-laden GelMA. The GelMA matrix was represented via user-defined material values of porosity (0.5) [31], and permeability (1×10^{-7}) [32]. The maximum amount of dissolvable oxygen was assumed to be $0.2185 \text{ (mol m}^{-3})$ [33], approximately representing oxygen dissolved in water. The consumption of oxygen by cells was represented as a decrease in oxygen species over time, following the equation, R = -kt, where R is the reaction rate (R < 0), k is the rate constant relating to oxygen concentration, and t is time in (s). The rate constant was determined to be 2×10^{-5} (mol s⁻¹) by taking into account the oxygen consumption rate of cells within each GelMA construct [34].

COMSOL was also used to model the changes in oxygen diffusion within cell-laden GelMA constructs due to mineral deposition around the lumen/channels. In this model, three domains were considered. Domain 1 represented the primary flow of nutrients supplied from the inlet reservoir and Domain 2 represented the diffusion of media and consumption by cells encapsulated within GelMA. A new Domain 3 was introduced in the form of a donut-shell and represented both regions of mineral deposition and cellladen GelMA. With more perfusion time, the thickness of Domain 3 increased and the porosity decreased due to an increasing amount of mineral deposition. The thickness of the donut-shell Domain 3 was obtained from ImageJ data, while the material porosity of Domain 3 (Pdonut-shell) at weeks 1, 2, and 4 was calculated as described below. The porosity of Domain 3 was a combination of (i) the porosity of the mineralized GelMA (identified from CT data) and (ii) the porosity of cell-laden GelMA (identified as void regions in CT data) given by the following equation (figures 6(B), (C)):

$$P_{\text{donut-shell}} = A * P_{\text{mineral}} + (1 - A) * P_{\text{GelMA}},$$

where A is the fraction of the donut-shell area occupied by mineralized GelMA and (1-A) is the remaining fraction that is occupied by cell-laden GelMA. Porosity of pure bone, $P_{mineral}$ (0.035) and cellladen GelMA P_{GelMA} (0.5) were obtained from previously published work [31, 35]. In this work, the inner channel radius was assumed to be 0.2 mm while the outer donut-shell radius for weeks 1, 2 and 4 were calculated as 0.2719 mm, 0.2854 mm and 0.2873 mm, respectively, from the BoneJ cortical thickness measurements of the mineralized crust. A, the fraction of donut-shell area occupied by the mineral, was calculated via a two-step process. First, CT data was imported into MIMICS (Materialise, Belgium), a Medical Image Processing software program, and 30 surface slices were generated for each time point and converted into 2D masks before being exported into ImageJ as binary (.stl) files. Second, the freehand boundary option in ImageJ was used to mark the irregular outer boundaries in each image to calculate the area occupied by mineral and void regions (area occupied by cell-laden GelMA). This data was then used to calculate Pdonut-shell for week 1, 2 and 4 (figure 6(D)).

Statistical analysis

Numerical data was entered into Microsoft Excel to calculate mean and standard deviation and either Student's *t*-test or one-way ANOVA was used to assess statistical significance of differences. *P*-values less than 0.05 were accepted as statistically significant.

Results

Design and fabrication of a plug-and-flow construct

Mechanically supportive ABS cages capable of housing GelMA hydrogels were printed using a commercially available 3D printer. Sacrificial PVA pipes were printed and inserted into holes within the ABS cage peripheries (white, figures 1(A), (B)). GelMA prepolymer was cast into the constructs and UV cured (figures 1(B), (C)) prior to the dissolution of the pipes (figure 1(C)). A fully customizable, two-piece plug-and-flow bioreactor fitted with a PDMS gasket was used to house the 3D printed constructs (figures 1(D)–(F), S1–2). Within the bioreactor base, the 3D printed constructs containing GelMA hydrogels could be press fit and perfused with DI water containing an orange food dye via a standard syringe pump. Flowed wells containing no constructs showed fluid-tight seals (figure 1(E) middle-top) while the well containing an ABS cage and GelMA hydrogel with dissolved pipe showed directed dye flow (figure 1(E) bottom).

All aspects of the plug-and-flow model process were capable of being fully sterilized using conventional techniques. Accordingly, the system was capable of being placed within a standard cell culture incubator for extended periods of time (figure 1(F)). Nutrients needed for cell viability were perfused through the constructs via a syringe pump placed within the incubator and gas exchange took place both through the tubing and a pressure relief needle in the waste collection area.

Perfusable GelMA laden hydrogels containing Saos-2 cells

In order to create cell-laden GelMA hydrogels containing encapsulated cells and fully perfusable pipes, Saos-2 cells were added to GelMA prepolymer and cast into the constructs. After curing, constructs were placed in cell culture media for 24 h prior to being placed in either well plates for static culture or the bioreactor for perfusion with osteogenic media (figure 2(A)). To determine if the plug-and-flow bioreactor represented a viable cell culture platform, cells were encapsulated around the dissolvable pipes and cultured for 24 h in order to determine process associated cell death. After one day of culture, minimal cell death was observed around the dissolved pipe (red, figure 2(B)). However, constructs perfused with osteogenic media for two weeks showed high cell viability (green, figure 2(C)) and significant mineral deposition around the entirety of the pipe (figure 2(D)). Micro-CT imaging was used to assess construct mineralization and showed mineral deposition surrounding the channel along the entire length of the construct (figure 2(E)).

Control experiments were run with cell-laden GelMA constructs without channels. Cells were encapsulated within ABS cages containing no dissolvable pipes and incubated for either 1 day or 14 days in osteogenic media (figure 2(F)). After 1 day of culture constructs were sectioned into 1 mm slices and showed low cell viability in the center of the hydrogel (red, figure 2(G)). After 14 days of static culture high cell death, in addition to a decreased number of cells, was observed (figure 2(H)) and no mineral appeared to form in the center of the hydrogel (figures 2(I), (J)).

Channel mineralization and modeling

Micro-CT was used to evaluate mineral formation around the construct channels under both static and dynamic conditions. Samples cultured within the bioreactor and perfused with osteogenic media for either 1 (P-W1), 2 (P-W2), or 4 (P-W4) weeks showed robust mineralization along the channel walls (figure 3(A), right). Solid samples containing no channels in static osteogenic culture showed mineral deposition around the construct periphery with no quantifiable activity within the center of the construct (figure 2(J)). Under the same conditions, constructs with channels were cultured in static osteogenic conditions for either 1 (S-W1), 2 (S-W2), or 4 (S-W4) weeks and showed increasing amounts of mineral deposition along the central pipe walls (figure 3(A), left). Additionally, in the static culture mineral was also deposited on the surface of the constructs, but appeared random and unordered. Furthermore, acellular control experiments showed no presence of mineral, indicating that the mineralization was completely mediated by encapsulated Saos-2 cells.

For mineral quantification, only the central channels of the constructs were digitally contoured in order to normalize comparisons between static and perfused samples (figure S3). Quantification of micro-CT data for the central channels of each construct showed that after one month of both static and perfusion culture, mineralization of the inner lumens increased significantly both volumetrically and in total mineral content for the 4 week samples as compared to their 1 and 2 week counterparts (figures 3(B), S4). Additionally, while the 2 and 4 week perfused constructs did not have significantly more mineral around their inner lumens as compared to their static equivalents, samples perfused for one week did have more mineral than those induced for one week in static culture. Furthermore, despite the increase in mineral content, the density of mineral formed was consistent among all samples at all time points, regardless of culture type (figure 3(C)).

To further characterize the constructs perfused within the bioreactor, BoneJ was used to analyze the micro-CT data to determine the average thickness of the mineral ring formed around the central channels (figure 6(D), table). While an upward trend in thickness could be inferred based on the data available, there was no statistically significant change as a function of time. Additionally, although total mineral content did increase significantly over the course of

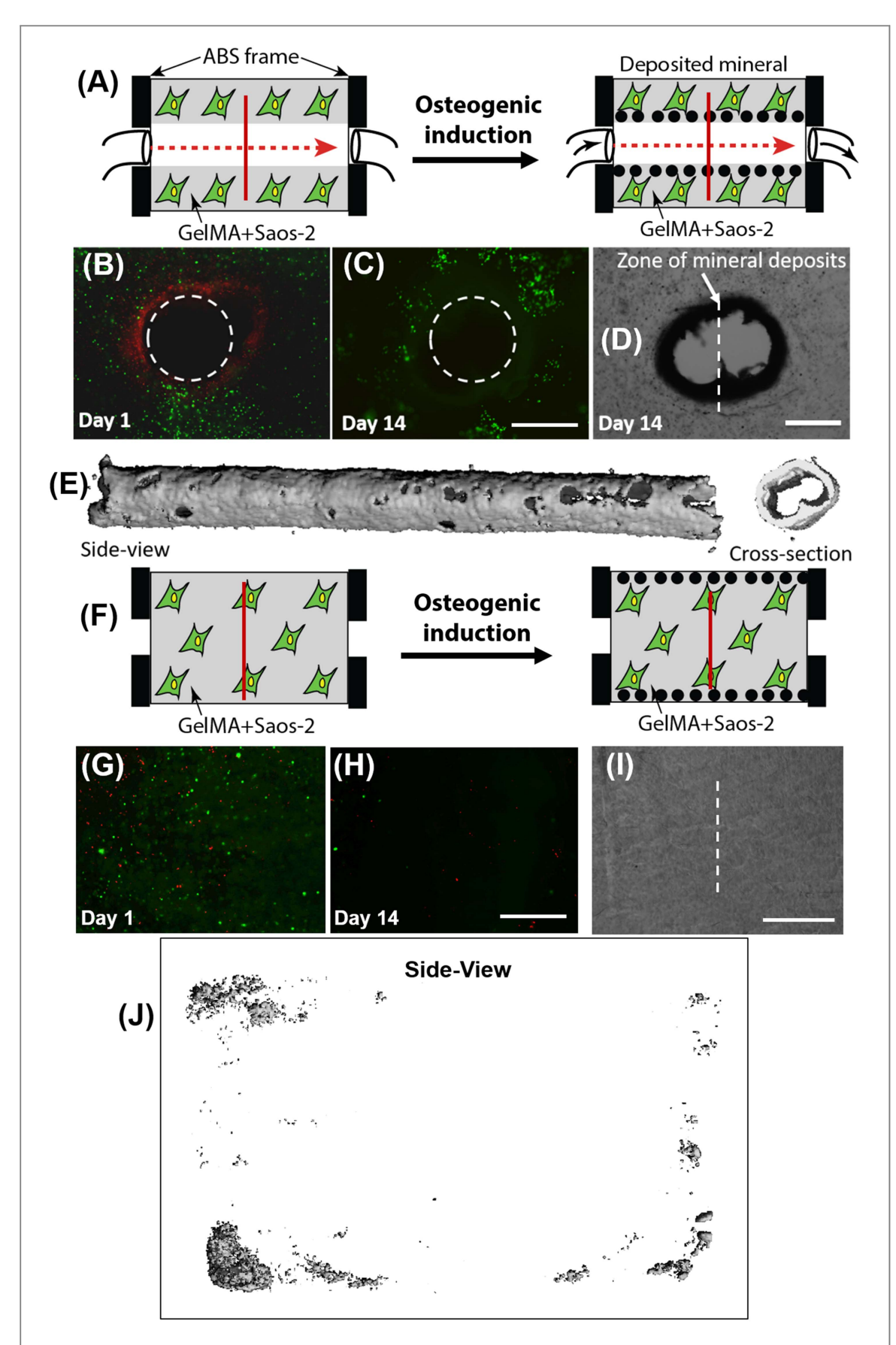


Figure 2. Perfusion can direct mineral deposition. Schematic representation of outcomes following osteogenic induction under (A) perfusion or (F) static culture conditions. Cell viability by fluorescent live (green)/dead (red) staining after perfusion (B), (C) or static culture (G), (H) conditions for either 1 (B), (G) or 14 days (C), (H), respectively. Brightfield microscopy showed an accumulation of an opaque matrix surrounding the perfused pipe (D) that was not evident in static constructs lacking a pipe (I) (scale bar: $400 \mu m$). Micro-CT imaging demonstrated mineral deposits surrounding the perfused pipe (E), whereas mineral accumulated only at the periphery of constructs maintained in static conditions (J).

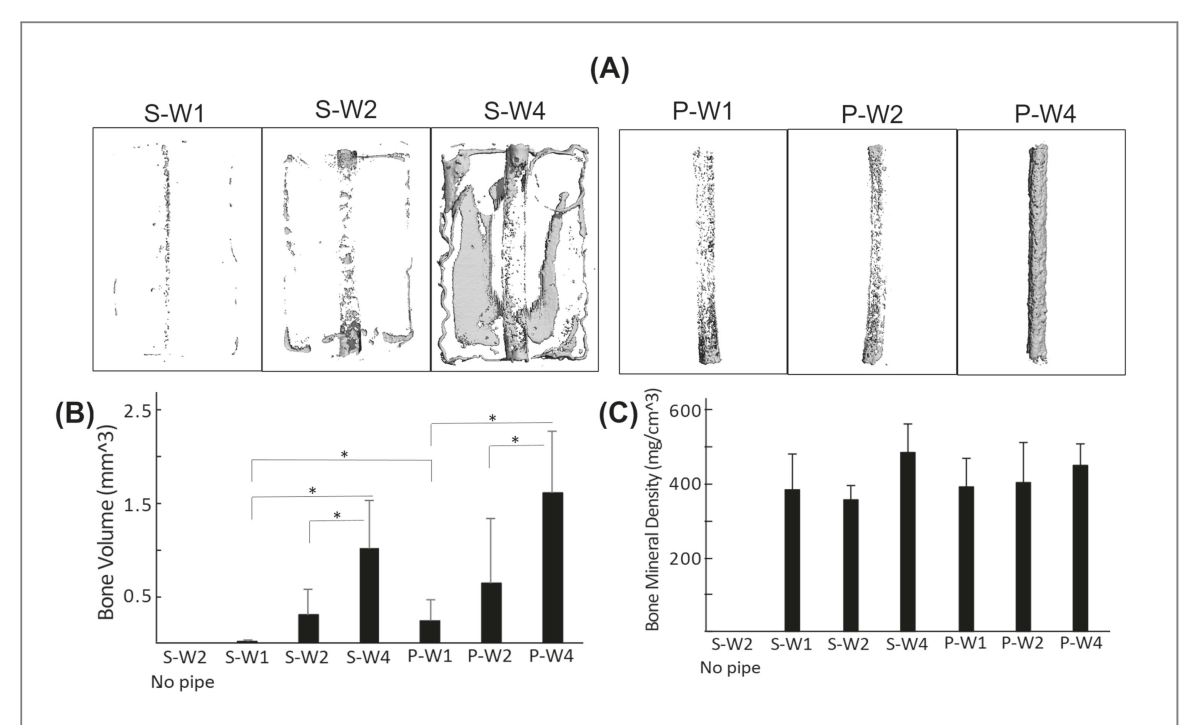


Figure 3. Representative micro-CT image of total mineral deposition after culture in osteogenic media under static (S) or perfused (P) conditions for 1, 2, or 4 weeks (A). For representative images, the entire frame was digitally contoured in order to visually show how mineralization occurs in static samples immersed in osteogenic media versus samples perfused directly with osteogenic media. Bone volume of mineral deposited around pipes after 1, 2, or 4 weeks of both static osteogenic culture and osteogenic media perfusion showed significant increases in volume after 4 weeks (4 wk static and 4 wk flow n = 7, 2 wk flow n = 8, rest n = 6. *p < 0.05) (B). Density of mineral deposited around pipe after 1, 2, or 4 weeks of both static osteogenic culture and osteogenic media perfusion remained constant at every time point (4 wk static and 4 wk flow n = 7, 2 wk flow n = 8, rest n = 6) (C).

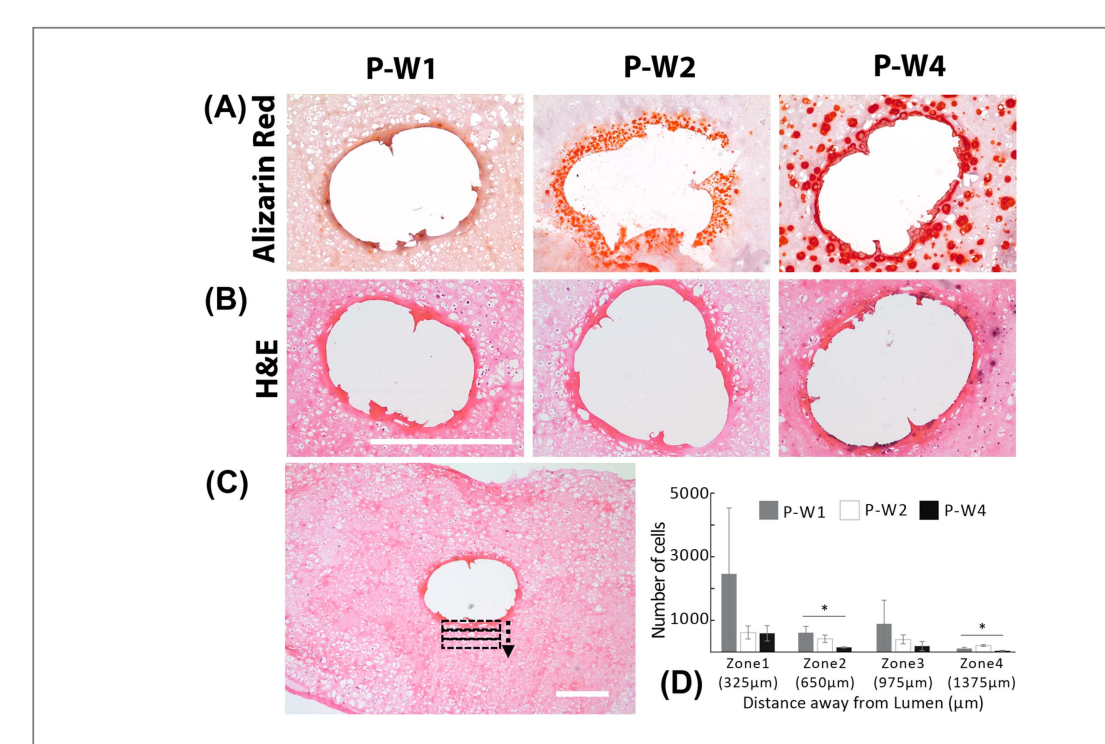


Figure 4. Cellular localization decreases and matrix mineralization increases as function of distance from the perfused channels. Representative Alizarin red (A) and H&E (B) histology stains of construct samples after either 1, 2, or 4 weeks of perfusion with osteogenic media (scale bar: 500 μ m). Box plot analysis of H&E samples was used to measure cell number in measured increments away from the central pipe (scale bar: 325 μ m) (C). Box plot quantification of the number of cells as a function of distance away from the lumen for 1, 2 and 4 week perfused samples shows that cell number decreases as the distance from the perfused channel increases (n=3, *p<0.05).

4 weeks for the perfused samples, the high variability in data, as well as the fact that the total mineral formed was not significantly greater in the 2 and 4 week perfused samples as compared to their static counterparts (figure S4), suggested that an increasing crust thickness could be inhibiting diffusion into the surrounding hydrogel matrix.

Histological analysis and quantification

Alizarin red S staining was used to visualize whether the diffusion limitations affected mineralization away from the perfused pipes, as well as verify that the deposits observed by the micro-CT contained calcium. After one week of perfusion, a small amount of mineral was present away from the pipe (figure 4(A), P-W1). After two weeks of perfusion, an increase of mineral was observed away from the perfused lumen, but appeared to decrease to levels consistent with 1 week of flow as the distance increased towards the construct peripheries (figure 4(A), P-W2). After 4 weeks of perfusion, however, while the amount of mineral observed closest to the pipe did not appear to increase significantly, more robust staining was observed (figure 4(A), P-W-4). Additionally, a significant amount of mineral was detected further away from the pipe in the 4 week samples as compared to both the 1 and 2 week samples, indicating that hydrogel degradation may possibly have played a role in the ability of the Saos-2 cells to mineralize the matrix after long-term perfusion.

H&E staining was performed on the perfused samples to visualize differences in construct cellularity over time (figure 4(B)) and a box analysis was used to quantify what effect long-term diffusion had on the distribution of cells away from the channel lumen (figures 4(C), (D)). After one week of perfusion, a large number of cells were observed approximately 300 μ m away from the channel, a distance in accordance with diffusion limitation values as reported in the literature (figures 4(B), (D)) [36]. However, as the mineral crust increased over the course of 2 weeks to 1 month, the quantity of cells dropped significantly 300 μ m away from the pipe.

Construct scalability

To test the scalability of this plug-and-flow approach, an array of 5 dissolvable PVA pipes within a larger ABS construct ($11 \times 8 \times 6$ outer dimension; $6 \times 6 \times 6$ inner dimension) was 3D printed. The optimal pipe spacing in the larger construct was chosen based on COMSOL simulations of the radial consumption of oxygen around the channels within the cell-laden GelMA matrix (figures 5(A), (B)). Specifically, COMSOL simulations showed that the addition of a second pipe spaced 1 mm away would ensure that the lowest oxygen concentration anywhere between the pipes would be approximately 80%, as opposed to 50% and below with only one channel (figures 5(A)–(C)).

Additionally, the design criteria were chosen to allow for the uncured cell-laden GelMA to conformably flow between the pipes, thereby ensuring there were no air pockets left between the pipes after UV exposure. Based on the analysis, it was determined that 400 μ m channels spaced approximately 1 mm apart (edge-to-edge) would ensure that the entire hydrogel matrix between the channels would be adequately supplied with nutrients (figures 5(C), (D)).

The pipes were placed in three layers spaced at least 1 mm apart in any direction (figure 5(D)) and the larger construct contained two reservoirs to ensure that all 5 pipes could be perfused via one syringe pump (figure 5(E)). In order to flow media through the larger system, the original bioreactor design was increased only in the *z*-direction to highlight the ease of scaling (figure 5(F)). After 4 weeks of perfusion, micro-CT and alizarin staining showed robust cell-associated mineral deposition along the length of each pipe, as well as between the pipes and along the edges of the bulk construct (figures 5(G)–(I)).

Estimation of the influence of mineral formation on oxygen diffusion

Based on the micro-CT results, it was clear that the mineral deposited by the encapsulated cells around the channel was not uniform (figure 6(A)). The annular ring of mineralized crust (figures 6(B), (C)) was porous with several void spaces that contained cell-laden GelMA. To gain insight into the spatial changes in oxygen diffusion due to the deposited mineralized 'donut-shell' around the channels, a new COMSOL Domain 3 (figure 6(C)) was introduced in the form of a 'donut-shell' with thickness values obtained from BoneJ data, and material porosity ($P_{donut-shell}$) values calculated as described in the Methods section (figure 6(D)). The results were plotted as percent decrease in oxygen concentration radially away from the channel/lumen edge (figure 6(E)). The results demonstrate that a higher drop in oxygen concentration is possibly due to the formation of mineral. This simulation provides qualitative explanation of the observed experimental results.

Discussion

Provision of adequate vascular perfusion is one of the most daunting challenges facing the manufacturing of any tissue engineered construct [37, 38]. Accordingly, over the past decade numerous groups have successfully combined various techniques and sacrificial materials such as pluronics, 3D printed carbohydrates, and 3D printed gels to create vascularized systems, but in each case the process used was extremely specific to the application being studied [20, 39, 40]. In our plugand-flow system, however, any component can be readily exchanged and scaled based on the desired application. For instance, the model cell could be

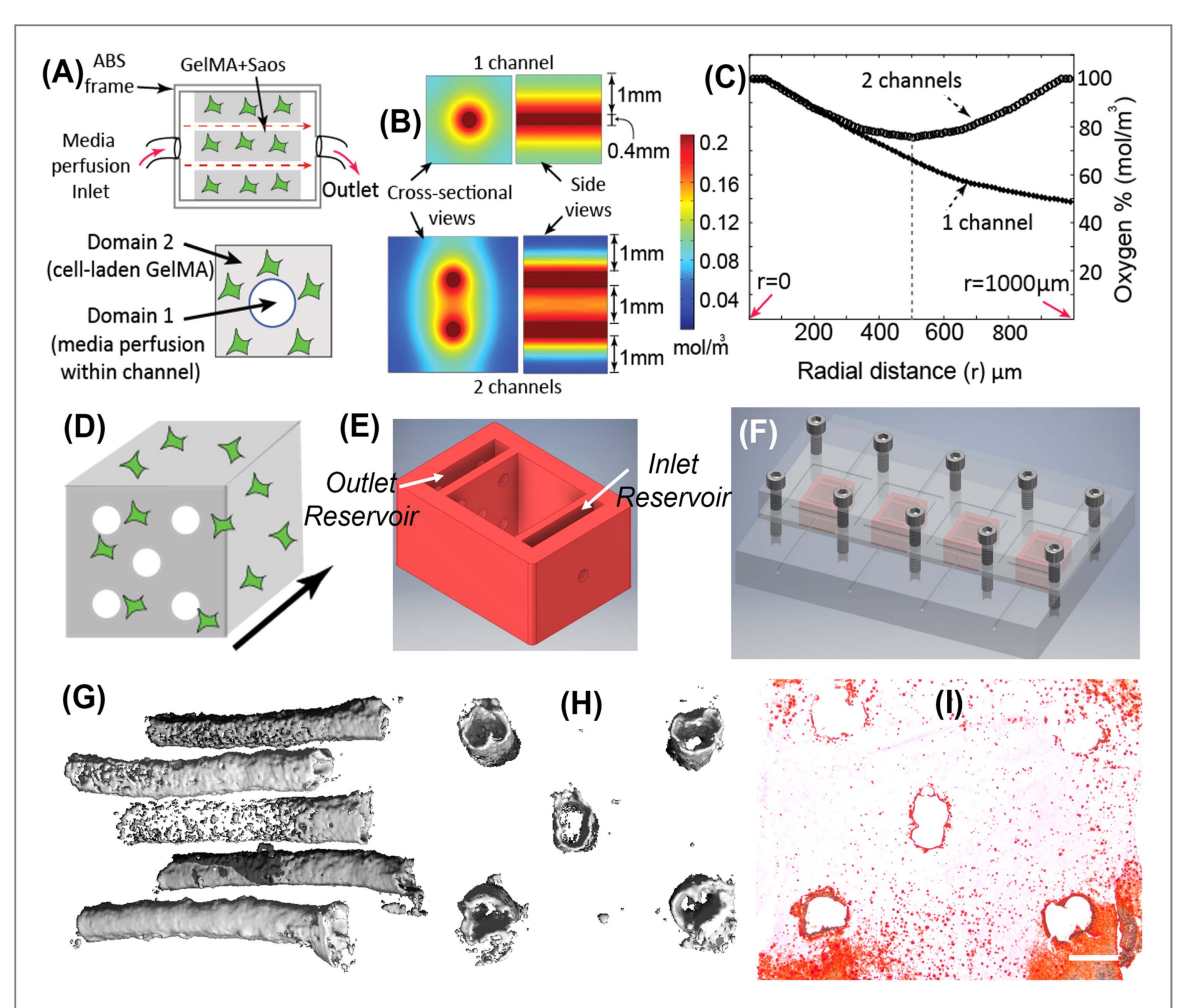


Figure 5. Schematic representing the scalability of perfusable constructs. Multiple channels spaced at optimal distances are capable of being perfused via one inlet (A). COMSOL modeling of oxygen diffusion between one channel (B top) and two channels spaced 1 mm apart (B bottom), as well as COMSOL modeling of the radial oxygen consumption by cells around the channels within cell-laden constructs spaced 1 mm apart (C) was used to determine optimal pipe spacing in larger constructs. Schematic of a scaled cell-laden construct (D) and corresponding ABS cage ($6 \times 6 \times 6 \text{ mm}^3$) (E). CAD isometric view of a machined, two-piece polycarbonate bioreactor containing a PDMS gasket between layers (red) (F). Micro-CT imaging of mineral deposition surrounding pipes ((G), side view; (H) Cross-sectional view) after four weeks of perfusion with osteogenic media showed that the model system could be easily scaled. Representative Alizarin Red histology of a large-scale construct after perfusion with osteogenic media for 4 weeks showed robust mineralization (scale bar: 500 μ m).

replaced with any other osteogenic cell such as patient-derived multipotent marrow stromal cells or autologous osteoblasts. Alternatively, the printed hydrogel could be easily modified via the addition of side groups and growth factors, or could be substituted for a different hydrogel altogether. Furthermore, due to the recent advances in 3D printing technology, numerous different hard and soft materials could be printed simultaneously, allowing for multiple cell types and complex vasculature to be easily incorporated during a single print using only slight modifications to our approach.

For this work, GelMA was chosen as our model hydrogel to encapsulate cells as it is a collagen derivative which possess RGD groups necessary for cell adhesion, contains readily tunable mechanical properties, and exhibits high structural integrity for experiments lasting over one month [41, 42]. Additionally, previous work has shown that GelMA properties such as diffusion, swelling, compressive moduli, and degree

of crosslinking are highly consistent between batches, allowing for the reduction of outside variables when conducting experiments [43-45]. Furthermore, GelMA is capable of being UV crosslinked with minimal negative side effects to the encapsulated cells [46, 47]. PVA was chosen to be the sacrificial material and ABS was chosen to be the structural frame for our model system due to the fact that they both are commercially available, biocompatible thermoplastics capable of being printed at high fidelities using common 3D printers. The selection of PVA allows for the possibility of printing user-defined channel-patterns for more complex tissue structures. Additionally, post-processing removal of PVA from the system is also simplified as PVA is water soluble, thereby reducing the possibility for external contaminants to be introduced into the system via manual pipe removal. In this model a flow rate of 0.2 ml h^{-1} was used, a rate well below what would be needed in a larger construct containing primary cells [48-50]. The decision to use

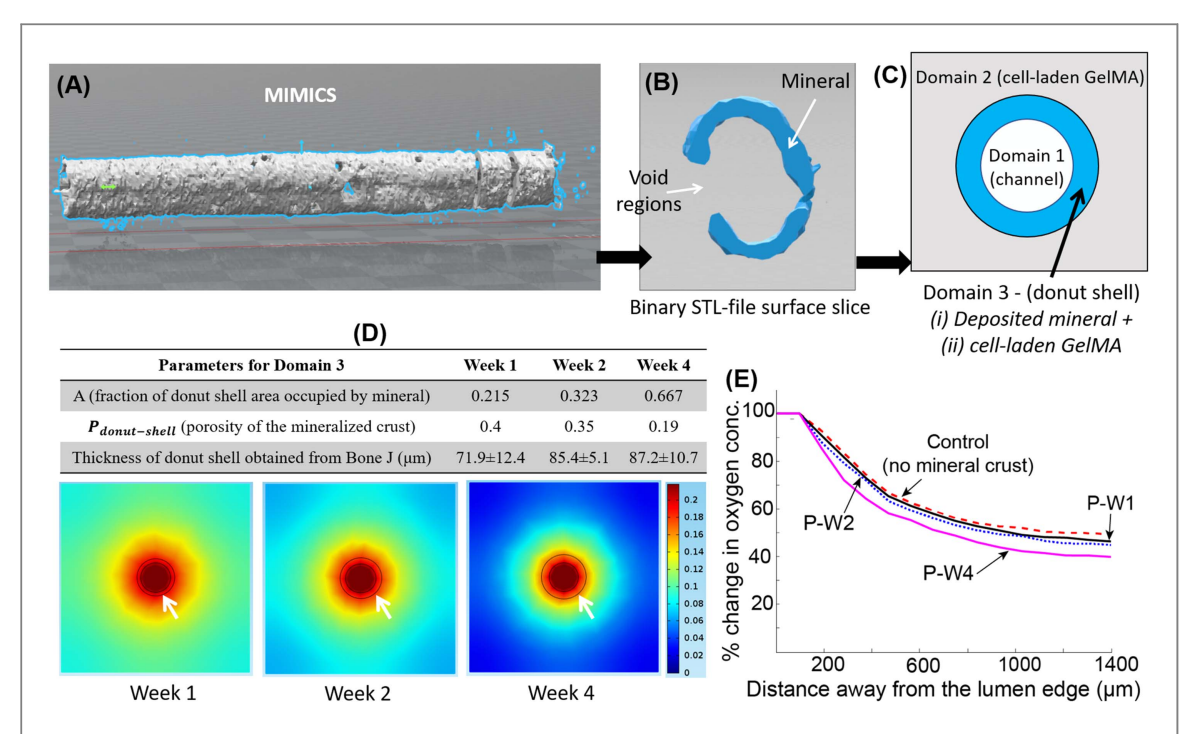


Figure 6. Effect of mineral formation on oxygen diffusion radially across the channel. Surface slices were obtained from 3D data sets in MIMICS, and mineral area was measured (A), (B). A schematic model showing the three domains used for COMSOL modeling (C). Table shows the various parameters used to calculate Domain 3 ((D), top table). Simulation of oxygen diffusion for weeks 1, 2 and 4 ((D), bottom; white arrows showing the donut-shell thickness). Distribution of oxygen radially away from the channel surface for weeks 1, 2 and 4 along with control without any mineral deposits (E).

this lower rate was made, however, based on previous work that has shown how higher flow rates in *in vitro* bioreactor systems have led to significant increases in cell death and reduced cell proliferation [51]. However, as the flow in this system is driven by a programmable syringe pump, further studies would easily be able to address this issue.

It is known that fully mineralized bone (in this case mineralized GelMA) is conducive to the diffusion of small solutes through interstitial spaces, albeit in the sub-nanometer range that cannot be observed with the micro-CT voxel resolution used. Additionally, even after 2 and 4 weeks of perfusion, we observed large voids in the deposited mineral (figure 2(E)) which were likely filled with cell-laden GelMA, thereby allowing for the diffusion of oxygen and other nutrients even after the formation of the mineralized crust. From the Live/Dead results (figure 2(C)), live cells could be seen outside the mineralized crust, indicating that diffusion of essential nutrients takes place even after mineral formation. However, the crust does possibly inhibit the oxygen concentration away from the perfused pipes to a degree, as was qualitatively explained via COMSOL modeling (figure 6).

This work represents a simple 'living' bioreactor system capable of creating mineral only around perfusable channels. However, more work needs to be performed to create a completely mineralized thick bone construct. The modularity of this model system allows for the incorporation of other cell types as well as the perfusion of growth factors with pulsatile perfusion conditions. One promising direction to enhance

overall mineral formation is the co-encapsulation of vascular endothelial cells with bone cells in this system to facilitate the formation of perfusable microvasculature between printed channels. Increased perfusion rates as well as the incorporation of pulsatile flow and specific growth factors can also be optimized within this model system. While long-term studies building upon the foundation of this model are necessary, this work provides early evidence that 3D printed, cell-laden hydrogels containing user-defined channels can be used as a model system for bone tissue engineering applications.

Conclusions

Our study demonstrated that user-defined 3D printed channels could be used to control mineral deposition within a diffusion-limited environment using commonly available 3D printers, sacrificial materials, and hydrogels. Based on these results, we anticipate that this technology could be easily scaled and reproduced in order to create thick, cell-laden constructs capable of serving as vascularized bone tissue substitutes, as well as be translated to other tissue engineering applications.

Acknowledgments

This work was supported by the CMMI 1547095, and (IGERT) DMR-DGE-1068780 at Syracuse University, funded by the National Science Foundation (NSF).

Author contribution

SWS and PS wrote the manuscript; SWS, JH, and PS conceived and designed the experiments; LA and AF machined perfusion bioreactors and 3D printed constructs; SWS and KZ performed cell studies and analyzed results; SVS simulated oxygen diffusion.

ORCID iDs

Stephen W Sawyer https://orcid.org/0000-0002-4453-0957

Pranav Soman https://orcid.org/0000-0001-9456-0030

References

- Bae H, Puranik A S, Gauvin R, Edalat F, Carrillo-Conde B, Peppas N A and Khademhosseini A 2012 Building vascular networks. Science translational medicine Sci. Trans. Med. 4 160ps23
- [2] Kaully T, Kaufman-Francis K, Lesman A and Levenberg S 2009 Vascularization—the conduit to viable engineered tissues *Tissue Eng.* B 15 159–69
- [3] Nichol J W and Khademhosseini A 2009 Modular tissue engineering: engineering biological tissues from the bottom up Soft Matter 5 1312–9
- [4] Lovett M, Lee K, Edwards A and Kaplan D L 2009 Vascularization strategies for tissue engineering *Tissue Eng.* B 15 353–70
- [5] Volkmer E, Drosse I, Otto S, Stangelmayer A, Stengele M, Kallukalam B C, Mutschler W and Schieker M 2008 Hypoxia in static and dynamic 3D culture systems for tissue engineering of bone *Tissue Eng.* A 14 1331–40
- [6] Yeatts A B and Fisher J P 2011 Bone tissue engineering bioreactors: dynamic culture and the influence of shear stress *Bone* 48 171–81
- [7] Hutmacher D W 2000 Scaffolds in tissue engineering bone and cartilage $\it Biomaterials\,21\,2529-43$
- [8] Mikos A G and Temenoff J S 2000 Formation of highly porous biodegradable scaffolds for tissue engineering *Electron. J. Biotechnol.* 3 23–4
- [9] Loh Q L and Choong C 2013 Three-dimensional scaffolds for tissue engineering applications: role of porosity and pore size *Tissue Eng. B* 19 485–502
- [10] Smith I, Liu X, Smith L and Ma P 2009 Nanostructured polymer scaffolds for tissue engineering and regenerative medicine Wiley Interdiscip. Rev.: Nanomed. Nanobiotechnol. 1 226–36
- [11] Hutmacher D W, Sittinger M and Risbud M V 2004 Scaffoldbased tissue engineering: rationale for computer-aided design and solid free-form fabrication systems *Trends Biotechnol.* 22 354–62
- [12] Annabi N, Tamayol A, Uquillas J A, Akbari M, Bertassoni L E, Cha C, Camci-Unal G, Dokmeci M R, Peppas N A and Khademhosseini A 2014 25th anniversary article: Rational design and applications of hydrogels in regenerative medicine Adv. Mater. 26 85–124
- [13] Antoniac I, Billiet T, Vandenhaute M, Schelfhout J, Vlierberghe S and Dubruel P 2013 Exploring the future of hydrogels in rapid prototyping: a review on current trends and limitations Biologically Responsive Biomaterials for Tissue Engineering vol 1 (New York: Springer) pp 201–49
- [14] Khademhosseini A and Langer R 2007 Microengineered hydrogels for tissue engineering *Biomaterials* 28 5087–92

- [15] Lee K and Mooney D 2001 Hydrogels for tissue engineering Chem. Rev. 101 1869–79
- [16] Slaughter B V, Khurshid S S, Fisher O Z, Khademhosseini A and Peppas N A 2009 Hydrogels in regenerative medicine Adv. Mater. 21 3307–29
- [17] Tibbitt M W and Anseth K S 2009 Hydrogels as extracellular matrix mimics for 3D cell culture *Biotechnol. Bioeng.* 103 655–63
- [18] Kloxin A M, Tibbitt M W and Anseth K S 2010 Synthesis of photodegradable hydrogels as dynamically tunable cell culture platforms Nat. Protocols 5 1867–87
- [19] Lewis K J and Anseth K S 2013 Hydrogel scaffolds to study cell biology in four dimensions MRS Bull. 38 260–8
- [20] Kolesky D B, Homan K A, Skylar-Scott M A and Lewis J A 2016 Three-dimensional bioprinting of thick vascularized tissues Proc. Natl Acad. Sci. 113 3179–84
- [21] Zhang Y, Yu Y, Chen H and Ozbolat I T 2013 Characterization of printable cellular micro-fluidic channels for tissue engineering *Biofabrication* 5 025004
- [22] Wüst S, Müller R and Hofmann S 2015 3D Bioprinting of complex channels—Effects of material, orientation, geometry, and cell embedding J. Biomed. Mater. Res. A 103 2558–70
- [23] Duan B 2017 State-of-the-art review of 3D bioprinting for cardiovascular tissue engineering Ann. Biomed. Eng. 45 195–209
- [24] Elomaa L and Yang Y P 2017 Additive manufacturing of vascular grafts and vascularized tissue constructs *Tissue Eng.* B 23
- [25] Arcaute K, Mann B K and Wicker R B 2006 Stereolithography of three-dimensional bioactive poly (ethylene glycol) constructs with encapsulated cells Ann. Biomed. Eng. 34 1429–41
- [26] Bajaj P, Schweller R M, Khademhosseini A, West J L and Bashir R 2014 3D biofabrication strategies for tissue engineering and regenerative medicine Annu. Rev. Biomed. Eng. 16 247–76
- [27] Raman R and Bashir R 2015 Stereolithographic 3D bioprinting for biomedical applications *Essentials of 3D Biofabrication and Translation* (Amsterdam: Elsevier) pp 89–121
- [28] Albrecht L D, Sawyer S W and Soman P 2016 Developing 3D scaffolds in the field of tissue engineering to treat complex bone defects 3D Print. Additive Manuf. 3 106–12
- [29] Rodan S B, Imai Y, Thiede M A, Wesolowski G, Thompson D, Bar-Shavit Z, Shull S, Mann K and Rodan G A 1987 Characterization of a human osteosarcoma cell line (Saos-2) with osteoblastic properties Cancer Res. 47 4961–6
- [30] Doube M, Kłosowski M M, Arganda-Carreras I, Cordelières F P, Dougherty R P, Jackson J S, Schmid B, Hutchinson J R and Shefelbine S J 2010 BoneJ: free and extensible bone image analysis in ImageJ Bone 47 1076–9
- [31] Athirasala A, Lins F, Tahayeri A, Hinds M, Smith A J, Sedgley C, Ferracane J and Bertassoni L E 2017 A novel strategy to engineer pre-vascularized full-length dental pulp-like tissue constructs Sci. Rep. 7 3323
- [32] Kipnis D M and Cori C V 1959 Studies of tissue permeability. V. The penetration and phosphorylation of 2-deoxyglucose in the rat diaphragm. J. Biol. Chem. 234 171–7
- [33] Chapra S C 2008 Surface Water-Quality Modeling (Long Grove, IL: Waveland Press)
- [34] Heppenstall R B, Grislis G and Hunt T K 1975 Tissue gas tensions and oxygen consumption in healing bone defects Clin. Orthopaedics Relat. Res. 106 357–65
- [35] Renders G, Mulder L, Van Ruijven L and Van Eijden T 2007 Porosity of human mandibular condylar bone J. Anat. 210 239–48
- [36] Mercado-Pagán Á E, Stahl A M, Shanjani Y and Yang Y 2015 Vascularization in bone tissue engineering constructs Ann. Biomed. Eng. 43 718–29
- [37] Lee J B, Wang X, Faley S, Baer B, Balikov D A, Sung H J and Bellan L M 2016 Development of 3D microvascular networks

- within gelatin hydrogels using thermoresponsive sacrificial microfibers *Adv. Healthcare Mater.* **5** 781–5
- [38] Bertassoni L E, Cecconi M, Manoharan V, Nikkhah M, Hjortnaes J, Cristino A L, Barabaschi G, Demarchi D, Dokmeci M R and Yang Y 2014 Hydrogel bioprinted microchannel networks for vascularization of tissue engineering constructs Lab Chip 14 2202–11
- [39] Miller J S, Stevens K R, Yang M T, Baker B M, Nguyen D-H T, Cohen D M, Toro E, Chen A A, Galie P A and Yu X 2012 Rapid casting of patterned vascular networks for perfusable engineered three-dimensional tissues Nat. Mater. 11 768–74
- [40] Byambaa B, Annabi N, Yue K, Trujillo-de Santiago G, Alvarez M M, Jia W, Kazemzadeh-Narbat M, Shin S R, Tamayol A and Khademhosseini A 2017 Bioprinted osteogenic and vasculogenic patterns for engineering 3D bone tissue Adv. Healthcare Mater. 6 1700015
- [41] Chen Y X, Yang S, Yan J, Hsieh M-H, Weng L, Ouderkirk J L, Krendel M and Soman P 2015 A novel suspended hydrogel membrane platform for cell culture J. Nanotechnol. Eng. Med. 6 021002
- [42] Sawyer S, Oest M, Margulies B and Soman P 2016 Behavior of encapsulated Saos-2 cells within gelatin methacrylate hydrogels J. Tissue Sci. Eng. 7 2
- [43] Yue K, Trujillo-de Santiago G, Alvarez M M, Tamayol A, Annabi N and Khademhosseini A 2015 Synthesis, properties, and biomedical applications of gelatin methacryloyl (GelMA) hydrogels *Biomaterials* 73 254–71

- [44] Chen Y X, Cain B and Soman P 2017 Gelatin methacrylatealginate hydrogel with tunable viscoelastic properties Aims Mater. Sci. 4 363–9
- [45] Sawyer S W, Dong P, Venn S, Ramos A, Quinn D, Horton J A and Soman P 2017 Conductive gelatin methacrylate-poly (aniline) hydrogel for cell encapsulation *Biomed. Phys. Eng. Express* 4 015005
- [46] Kumar D, Gerges I, Tamplenizza M, Lenardi C, Forsyth N R and Liu Y 2014 Three-dimensional hypoxic culture of human mesenchymal stem cells encapsulated in a photocurable, biodegradable polymer hydrogel: a potential injectable cellular product for nucleus pulposus regeneration Acta Biomater. 10 3463–74
- [47] Chung C, Mesa J, Randolph M A, Yaremchuk M and Burdick J A 2006 Influence of gel properties on neocartilage formation by auricular chondrocytes photoencapsulated in hyaluronic acid networks J. Biomed. Mater. Res. A 77 518–25
- [48] Buckwalter J, Glimcher M, Cooper R and Recker R 1995 Bone biology *J. Bone Joint Surg. Am.* 77 1256–75
- [49] McCarthy I 2006 The physiology of bone blood flow: a review *J. Bone Joint Surg.* **88** (Suppl. 3) 4–9
- [50] Laroche M 2002 Intraosseous circulation from physiology to disease *Joint Bone Spine* 69 262–9
- [51] Cartmell S H, Porter B D, García A J and Guldberg R E 2003 Effects of medium perfusion rate on cell-seeded threedimensional bone constructs in vitro Tissue Eng. 9 1197–203